Engineering corrosion protection: the critical link between MgO nanoparticles synthesis and inhibition mechanism

Lingru Zhong [a], Oksana Dubinina [a,*].

a. Division for Material Science, School of Advanced Manufacturing Technologies, Tomsk Polytechnic University, Lenina Avenue 30, 634050 Tomsk, Russia

*Corresponding author: dubininaov@tpu.ru

Keywords

Magnesium oxide nanoparticles;
Microwave-assisted synthesis;
Sol-gel synthesis;
Carbon steel corrosion;
Corrosion inhibition;
Electrochemical analysis;
Nanoparticle morphology.

Abstract

This study investigates the influence of synthesis methodology on the structural characteristics and corrosion inhibition performance of MgO nanoparticles for carbon steel 65 Mn. Nanopowders were synthesized via two contrasting routes: rapid microwave-assisted synthesis (MAS) and protracted sol-gel synthesis (S-GS). Comprehensive characterization revealed that MAS produced smaller, defect-rich nanoparticles with a higher impurity content, whereas S-GS yielded larger, more stoichiometric particles with superior phase purity. Corrosion inhibition efficiency was evaluated in 0.1 M HCl and 0.1 M NaCl environments using gravimetric and electrochemical techniques. Electrochemical impedance spectroscopy confirmed the formation of a more protective surface layer by the purer S-GS-MgO. The results establish a critical *structure-property-performance* triad, demonstrating that the synthesis pathway is a primary design parameter dictating phase purity and particle architecture, which in turn govern the dominant inhibition mechanism – from barrier formation in acid to interfacial pH modification in neutral media. The work validates a critical *structure-property-performance* triad, providing a foundational framework for the rational design of nano-inhibitors targeted for specific corrosive threats.

Highlights

- Synthesis pathway is a decisive design parameter for MgO nano-inhibitors, directly governing their structure and properties.
- A critical structure–property–performance triad was established, linking synthesis to the protective mechanism.
- The inhibition mechanism shifts from barrier formation in acid to barrier-plus-passivation via interfacial pH modification in neutral chloride media.

1. Introduction

Corrosion is not merely a materials degradation process; it is a fundamental thermodynamic recalibration, a relentless drive of engineered metals to revert to their natural, oxidized states. This silent war of attrition against metallic infrastructure costs the global economy trillions annually and poses persistent safety and environmental challenges [1]. While the battle has traditionally been fought with molecular-scale inhibitors – organic compounds and toxic chromates – their efficacy is often constrained by environmental persistence, limited stability, and increasing regulatory scrutiny [2, 3]. A paradigm shift is emerging from the nano-realm, where inorganic nanoparticles are not simply additives but active, multi-functional agents that redefine the interface between a metal and its hostile environment [4, 5].

Within this new arsenal, magnesium oxide nanoparticles present a compelling paradox. As a basic anhydride, MgO is inherently antagonistic towards acidic corrodes, yet its nanoscale incarnation offers a unique blend of reactivity and stability that can be harnessed for protection [6]. The prevailing literature often treats nano-inhibitors as monolithic entities, reporting performance metrics without fully deconvoluting the intricate interplay between synthetic genesis and ultimate function [7, 8]. This overlooks a critical axiom in nanoscience: *a nanoparticle's identity and efficacy are born in the crucible of its synthesis*. The method of creation – be it through the rapid, kinetically-controlled chaos of microwave irradiation or the thermodynamically-guided, deliberate assembly of sol-gel chemistry – imprints an indelible signature on particle size, morphology, crystallinity, and most notably, surface defect chemistry and phase purity [9, 10]. These characteristics are not ancillary; they are the very determinants of interfacial behavior, adsorption kinetics, and barrier formation mechanics [11].

This study focuses on carbon steel 65 Mn, a medium-carbon, manganese-enhanced spring steel widely employed in demanding mechanical applications such as high-stress springs, railway components, and agricultural tools due to its favorable combination of strength, toughness, and wear resistance. However, its operational environments often involve exposure to acidic condensates, industrial atmospheres, or chloride-containing media, making it susceptible to both uniform and localized corrosion. Investigating the efficacy of nano-inhibitors on this technologically relevant alloy therefore bridges a critical gap between fundamental nanoparticle design and practical corrosion mitigation in industrial sectors where material failure carries significant economic and safety consequences.

The current narrative on nano-MgO inhibitors frequently focuses on a single synthesis route or a binary performance outcome, leaving a significant knowledge gap regarding a direct, causal comparison of how fundamentally different synthetic philosophies manifest in corrosion inhibition mechanisms [12, 13]. Does the ultrafine, defect-rich landscape of a microwave-synthesized nanoparticle, potentially riddled with metastable phases and impurities, confer an advantage through higher surface energy and reactivity? Or does the larger, more stoichiometric and ordered particle produced by sol-gel methods provide a superior, more stable physical barrier? The answer is not monolithic and likely depends on the electrochemical nature of the threat – be it the proton-driven assault of acidic media or the insidious, localized attack chloride ions orchestrate in neutral environments [14, 15].

This study posits that the choice of synthesis pathway is a primary design parameter, not merely a preparatory step. We argue that to truly engineer an effective nano-inhibitor, one must first engineer its creation. To test this hypothesis, we deliberately orchestrated a confrontation between two contrasting synthetic philosophies: the rapid, energy-dense microwave-assisted synthesis and the protracted, solution-based equilibrium of sol-gel synthesis. We then subject the resulting MgO nanopowders to a rigorous multi-modal interrogation – linking their structural fingerprints from XRD and TEM directly to their performance metrics in both acidic and neutral chloride environments through gravimetric and advanced electrochemical techniques.

This work moves beyond the conventional report of inhibition efficiency. It seeks to establish a *structure-property-performance* triad for MgO nano-inhibitors, providing a foundational framework for the rational selection and design of nanomaterials for targeted corrosion protection. By dissecting how synthesis-induced differences in phase purity and particle architecture dictate protective mechanisms – from barrier formation to potential interfacial pH modification – we aim to contribute a more nuanced, intellectually sophisticated blueprint for the next generation of corrosion inhibitors.

2. Experimental section

2.1. Materials

Carbon steel (CS) 65 Mn with the composition, presented in Table 1, was used for the studies.

2.1.1. Preparation of steel samples for corrosion studies

Square test coupons with surface areas of 1 cm² and 0.25 cm² were employed for weight loss measurements and electrochemical analyses, respectively. Prior to experimentation, the exposed surfaces of the carbon steel coupons were mechanically ground using a sequence of emery papers with progressively finer grit sizes P 400, P 600, P 1000 (ISO 6344). This preparatory grinding procedure was implemented to standardize the surface condition, thereby mitigating its potential influence on the assessment of corrosion inhibition performance. It is imperative to note that the duration and applied pressure during the grinding process were maintained as consistent as possible across all specimens to ensure uniformity in surface preparation.

2.1.2. Preparation of magnesium oxide nanopowders (MgO)

In this investigation, MgO nanoparticles were synthesized by two methods: microwave-assisted synthesis (MAS) and sol-gel synthesis (S-GS).

2.1.3. Microwave-Assisted Synthesis of MgO nanoparticles

MgO nanoparticles were synthesized via a microwave-assisted method. Magnesium nitrate hexahydrate ($Mg(NO_3)_2 \cdot 6H_2O$) was employed as the precursor. A quantity of 1.8 g of the specified salt was dissolved in 100 ml of deionized water under constant stirring for 30 minutes (0.1 M precursor solution). A 0.1 M sodium hydroxide (NaOH) solution was subsequently added to the obtained clear precursor solution, resulting in the immediate formation of a white suspension, indicative of the precipitation of an intermediate product. The resulting suspension was subjected to microwave irradiation for a duration of 15 minutes. Upon completion of the reaction, the product was centrifuged for 10 minutes at 3000 rpm. The white precipitate was collected and repeatedly washed with deionized water and ethanol until a neutral pH (≈7) was attained to ensure the complete removal of ionic impurities. The final MgO nanoparticles were obtained by thermal treatment of the purified precipitate in a muffle furnace at 400 °C for 4 hours, followed by a 5-minute dwell time at room temperature.

2.1.4. Sol-Gel Synthesis of MgO nanoparticles

MgO nanoparticles were synthesized via a sol-gel method. Magnesium nitrate hexahydrate ($Mg(NO_3)_2 \cdot 6H_2O$) was employed as the precursor. A quantity of 1.8 g of the salt was dissolved in 100 ml of deionized water under constant stirring to obtain a clear 0.1 M precursor solution. The 0.1 M NaOH solution was then added to the precursor solution, leading to the immediate formation of a white suspension (sol). The suspension was continuously stirred for 5 hours to facilitate the aging process and complete gel formation. Following the aging process, the product was centrifuged for 10 minutes at 3000 rpm. The resulting precipitate was collected and sequentially washed with deionized water and ethanol until a neutral pH (≈7) was achieved to ensure the complete removal of reaction by-products and ionic impurities. The final stage of MgO nanoparticles synthesis was accomplished through thermal treatment of the purified precipitate in a muffle furnace. Calcination was performed at a temperature of 400 °C for 4 hours, followed by a dwell time of 5 minutes at room temperature.

2.1.5. Preparation of corrosion inhibitor suspensions

Corrosion inhibitor suspensions were formulated by dispersing magnesium oxide nanopowders in distilled water. The application of the inhibitors onto the carbon steel substrates was performed via a cotton swab to ensure a consistent coating, followed by air-drying under laboratory atmosphere.

2.1.6. Preparation of corrosive media

This study utilized three distinct corrosive media. Electrochemical analyses were conducted in 0.1 M hydrochloric acid (HCl) and 0.1 M sodium chloride (NaCl) solutions. Conversely, weight loss assays were performed in an acidic mixture comprising 67% nitric acid (HNO_3), 35% hydrochloric acid (HCl), and double-distilled water in a 3:2:5 volume ratio. All chemical reagents were sourced from Sigma-Tec (Russia) and were employed without further purification.

2.2 Methods of analysis

2.2.1. Granulometry

The particle size distribution of MgO nanopowders was determined via laser diffraction analysis using a SALD-7101 nanoparticle size analyzer (Shimadzu, Japan). This technique operates on the principle of static light scattering, wherein a sample dispersed in a liquid medium is exposed to a semiconductor laser beam (wavelength λ=375 nm) [16]. The angular dependence of the scattered light intensity was detected by a multi-element photodetector array. For analysis, a powder sample was dispersed in distilled water, which served as the dispersant liquid, within a flow cell. To ensure deagglomeration and a monodisperse state, the suspension was subjected to ultrasonic treatment for five minutes prior to measurement.

2.2.2. TEM

Transmission electron microscope (TEM) (JEOL JEM-2100F, Japan), operated at an accelerating voltage of 200 kV**,** employed to investigate the granulometry and morphology of MgO nanoparticles [17].

2.2.3. X-Ray Diffraction

The phase composition and crystal structure of the magnesium oxide nanopowders were characterized by X-ray diffraction (XRD). The measurements were performed using a Shimadzu XRD-7000 diffractometer (Shimadzu Corporation, Japan) operated with Cu $K\alpha$ radiation ($\lambda = 1.54056$ Å) generated by a copper anode X-ray tube [18]. The acquired diffraction patterns were used for phase identification by comparison with reference patterns from the ICDD (International Centre for Diffraction Data) JCPDS PDF-2 database.

2.2.4. Weight loss measurements

Gravimetric analysis, a standard method for evaluating material degradation, was employed to assess the corrosion resistance of carbon steel coupons [19]. This technique involves monitoring mass loss of specimens exposed to an aggressive environment over a defined period. Accelerated corrosion testing was conducted in an acidic solution of HNO_3:HCl:H_2O (3:2:5 volume ratio), with the mass of the CS coupons measured at five-minute intervals to track degradation kinetics.

The average corrosion rate ($\bar{v}$) was calculated from the following Eq. (1):

where m_0 is the mass of the sample before corrosion, m_i is the mass of the sample after corrosion, and t is the time at which corrosion occurs, S is the surface area of steel specimens (1 cm^2).

The corrosion inhibition efficiency of the corrosion inhibitor was calculated by Eq. (2):

where v_0 represents the average corrosion rate of the uninhibited CS control specimen, and v_i denotes the average corrosion rate of the CS specimen with the corrosion inhibitor.

2.2.5. Electrochemical analysis

Electrochemical measurements were conducted using a CS310 Potentiostat/Galvanostat electrochemical workstation (CorrTest Instruments, China) in accordance with standard potentiodynamic polarization techniques [20]. A conventional three-electrode electrochemical cell, fabricated from Pyrex glass, was employed for all experiments. The cell configuration consisted of a prepared carbon steel specimen (exposed surface area $S = 0.25$ cm^2) as the working electrode, a saturated silver chloride (Ag/AgCl) electrode as the reference electrode, and a second Ag/AgCl electrode serving as the auxiliary electrode. The electrolytes were 0.1 M HCl and 0.1 M NaCl solutions.

Prior to polarization, the working electrode was immersed in the electrolyte for 600 seconds to allow the open circuit potential (OCP) to stabilize. Potentiodynamic polarization curves were subsequently recorded by scanning the potential from -0.3 V to +0.3 V versus the OCP at a constant scan rate of 10 mV/s.

The corrosion inhibition efficiency (η_{pdp}) of the inhibitor was calculated from the corrosion current densities using the following Eq. (3):

$$\eta_{pdp} = \frac{(i_{corr(blank)} - i_{corr(inh)})}{i_{corr(blank)}} \times 100\% \tag{3}$$

where, η – the efficiency of corrosion inhibition; $i_{corr(blank)}$ – corrosion current density of CS without inhibitor; $i_{corr(inh)}$ – corrosion current density of CS with inhibitor.

The corrosion rate in mm/year was obtained by using Eq. (4):

$$v_{corr} = \frac{i_{corr} \times E_q}{\rho \times F} \tag{4}$$

where: i_{corr} – corrosion current density (A·cm^{-2}); E_q – chemical equivalent of the alloy (g·mol^{-1}); ρ – density of the alloy (g·cm^{-3}); F – Faraday's constant, 96500 C·mol^{-1}. The calculation results are recorded in mm/year after unit conversion.

Complementary electrochemical impedance spectroscopy (EIS) measurements were immediately conducted following the PDP tests without altering the electrode surface. EIS spectra were acquired in the frequency range from 10^3 Hz to 10^6 Hz with an applied sinusoidal perturbation amplitude of 10 mV. The resulting impedance data were analyzed and fitted to equivalent electrical circuit models using ZView software (Scribner Associates Inc., USA). To ensure reproducibility, a minimum of three to four independent measurements were performed for each condition, with the most representative dataset being selected for reporting [21].

For the fitting results of the constant phase angle element CPE, according to the report of Bryan Hirschorn et al. [22], the double-layer equivalent capacitance (C_{dl}) was calculated by applying the Brug's Eq. (5):

$$C_{dl} = Y_0^{1/n} \cdot R_s^{(1-n)/n} \tag{5}$$

where: C_{dl} – double-layer equivalent capacitance ($F \cdot cm^{-2}$); Y_0 and n – characteristic parameters of the constant phase angle element *CPE* are *CPE-T* ($S \cdot s^n \cdot cm^2$ or $Ohm \cdot s^{-n} \cdot cm^2$) and *CPE-P* obtained by fitting with ZView software; R_s – solution resistance ($Ohm \cdot cm^2$).

3. Results and Discussion

3.1 MgO powders characterization

The structural and phase characteristics of the synthesized MgO nanopowders were rigorously evaluated using XRD analysis, as presented in Figure 1. The diffractograms for both synthesis methods exhibit a series of sharp and well-defined diffraction peaks, indicative of a high degree of crystallinity within the powders. Phase identification was performed by indexing the observed diffraction lines against standard reference patterns from the ICDD JCPDS PDF-2 database. The predominant phase in both samples was confirmed to be MgO with a face-centered cubic crystal structure. The lattice parameter for the synthesized MgO was calculated to be $a = 0.4213$ nm, which is in excellent agreement with the standard reference value, confirming the successful formation of the target compound.

A critical observation from the XRD analysis is the presence of secondary diffraction peaks, which were identified as sodium nitrate ($NaNO_3$). The presence of this by-product is attributed to the incomplete removal of ionic species during the washing stage of the synthesis, likely originating from the reaction between NaOH precipitating agent and the nitrate (NO_3^-) anions from the magnesium precursor salt ($Mg(NO_3)_2 \cdot 6H_2O$). A semi-quantitative estimation based on the relative intensity of the major peaks revealed a notable difference in the impurity content between the two synthesis routes. The MgO nanopowder produced via the sol-gel method contained less than 5 wt.% $NaNO_3$, whereas the sample obtained via microwave-assisted synthesis contained approximately 15 wt.% of the impurity phase. This discrepancy can be rationalized by considering the reaction kinetics inherent to each method. The rapid and intense heating characteristic of microwave irradiation may lead to the rapid entrapment of sodium nitrate within the forming MgO matrix, making its subsequent removal via washing more challenging. In contrast, the prolonged aging period (5 hours) during the sol-gel process potentially allows for more Ostwald ripening and a more thermodynamically stable product, facilitating a more complete purification during the washing steps.

In conclusion, while both synthesis methods successfully produced crystalline MgO, the sol-gel technique yielded a product with higher phase purity. The presence of sodium nitrate, particularly in the microwave-synthesized sample, is a significant factor that must be considered, as surface impurities can profoundly influence the interfacial properties and, consequently, the performance of the nanopowders when applied as corrosion inhibitors. While nitrate anions can exhibit oxidizing properties and participate in cathodic reactions under certain conditions, their primary detrimental effect in this context is likely physical rather than electrochemical. As a water-soluble ionic salt, $NaNO_3$ embedded within the MgO matrix can lead to a porous and defective microstructure in the applied inhibitor layer. These defects compromise the barrier's cohesion and provide direct channels for electrolyte ingress, thereby reducing the overall protection efficiency. This aligns with established principles where secondary phases and impurities can act as sites for localized attack and film breakdown [23]. The superior performance of the higher-purity S-GS-MgO underscores the critical importance of phase purity for forming a coherent and effective protective film.

To investigate the morphology and size characteristics of the synthesized MgO nanopowders, transmission electron microscopy was employed. Figure 2 presents TEM micrographs and the corresponding particle size distribution histograms for the samples obtained via microwave-assisted synthesis (Fig. 2 a, b) and the sol-gel method (Fig. 2 c, d). Morphological analysis revealed that the particles in both samples exhibit an irregular, elongated strip-like morphology, approaching equiaxial shape. However, significant differences in size distributions were observed between the samples. Quantitative analysis of the TEM images demonstrated that the MgO nanopowder synthesized by the MAS method is characterized by significantly smaller particle sizes. The most probable (modal) particle size is 11 nm, with an average size of 15.72±0.12 nm. The particle size distribution is narrow and monomodal, with 49% of all particles falling within the 10-16 nm range. This homogeneity and nanoscale size are a direct consequence of the synthesis kinetics governed by microwave heating, which facilitates rapid and uniform nucleation and subsequent growth, thereby minimizing aggregation and Ostwald ripening processes.

In contrast, the sample synthesized by the S-GS method exhibits substantially larger particle sizes. The distribution is also monomodal but shifted towards larger particles: the modal size is 45 nm, and the average size is 62.7±0.2 nm. The vast majority of particles (71%) have sizes within the 50-70 nm range. The increase in particle size in this case is attributed to the prolonged sol aging time (5 hours), which provides conditions for pronounced Ostwald ripening – a process involving the dissolution of smaller particles and the growth of larger ones, leading to an increase in average size and a narrowing of the distribution.

Thus, the conducted analysis unequivocally demonstrates that the chosen synthesis method has a decisive influence on the size characteristics of the MgO nanopowders. Microwave-assisted synthesis yields ultrafine particles with a size of ~15 nm, whereas the sol-gel method, under the employed conditions, results in the formation of particles with a size of ~60 nm. This difference in dispersity may critically affect the specific surface area, adsorption capacity, and consequently, the corrosion inhibition efficiency of these nanomaterials in aggressive environments.

To evaluate the hydrodynamic size characteristics of the synthesized MgO particles in an aqueous medium, laser diffraction analysis (static light scattering) was employed. The volumetric particle size distributions for the aqueous suspensions of MgO-MAS and MgO-S-GS are presented in Figure 3, panels (a) and (b), respectively. Both distributions are unimodal. The MgO-MAS suspension (Fig. 3 a) exhibits a primary peak maximum in the range of 0.35-0.45 μm, with a modal size of 0.4 μm. In contrast, the MgO-S-GS suspension (Fig. 3 b) displays a significantly larger modal size of 6 μm, with the peak spanning 5.5-7 μm. Notably, these values represent a substantial increase – approximately an order of magnitude greater – compared to the primary particle sizes determined by TEM analysis (15.72 nm and 62.7 nm for MAS and S-GS, respectively). This pronounced discrepancy is attributed to the aggregation of primary nanoparticles upon dispersion in the aqueous medium. Collisions between particles lead to the formation of large aggregates, resulting in a broad overall size distribution ranging from 0.2 to 25 μm for both samples. Analysis of the laser diffraction data established the mean volumetric particle size, representative of these aggregates, to be approximately 0.5 μm for MgO-MAS and 8.2 μm for MgO-S-GS. These findings confirm that the powders form complex agglomerates in suspension, a critical factor influencing their interfacial behavior and application efficacy.

The significant disparity between the primary particle size (TEM) and the aggregate size in suspension (from laser diffraction) for both MgO types confirms pronounced agglomeration in the aqueous medium. This is a common challenge for high-surface-area oxide nanoparticles due to strong van der Waals forces and hydrogen bonding. The larger aggregate size of S-GS-MgO (~8.2 μm) compared to MAS-MgO (~0.5 μm) likely reflects the inherent tendency of its larger primary particles (~63 nm vs. ~16 nm) to form more settled aggregates, although the higher impurity content in MAS-MgO may also influence interparticle interactions.

This agglomerated state directly influences the interfacial processes relevant to corrosion inhibition. The aggregates, rather than isolated primary particles, are the functional units adsorbing onto the steel surface. The size and stability of these aggregates influence the morphology, coherence, and porosity of the formed protective layer. While the finer aggregate size of MAS-MgO might suggest the potential for a denser initial coating, its higher impurity content likely compromises the integrity and adhesion of the agglomerated layer, as discussed earlier. Conversely, the larger but purer S-GS-MgO aggregates appear to form a more stable and effective barrier, as evidenced by the electrochemical data. This suggests that the cohesion within the agglomerated layer and its chemical stability in the corrosive medium are more critical for protection than the primary particle size alone.

In this comparative study, no additional dispersion aids (e.g., surfactants or ultrasonic energy beyond the brief pre-measurement treatment) were employed to modify the agglomerated state. This approach was intentional to evaluate the performance of the as-synthesized powders in a simple aqueous suspension, reflecting a potential application scenario. Future work optimizing dispersion through chemical or physical means could further enhance performance by improving surface coverage and layer uniformity, thereby decoupling the effects of primary particle properties from aggregation state [24, 25]. However, within the present framework, the results underscore that the synthesis pathway dictates not only primary particle characteristics but also their aggregation behavior, both of which are integral to the final structure-property-performance triad.

While this study focused on the short-term protective performance, the long-term stability of the nanoparticle-based layer in corrosive environments is a critical practical consideration. The agglomeration state observed in suspension (Fig. 3) is likely dynamic under prolonged exposure. In acidic media, the partial chemical dissolution of MgO over time could alter the local porosity and cohesion of the barrier layer. Conversely, in neutral chloride media, the stability is expected to be higher due to the lower solubility of MgO. However, the localized pH increases at the interface, which is central to the inhibition mechanism, may itself influence agglomeration and sedimentation kinetics over extended periods. For the purer S-GS-MgO, the lower impurity content suggests a more chemically stable interface, potentially leading to more durable protection. Future work employing long-term immersion tests, in-situ monitoring of particle size distribution in electrolyte, and surface analysis of aged inhibitor layers is warranted to fully deconvolute these temporal effects and engineer nano-inhibitors with enhanced operational longevity.

3.2 Corrosion inhibition efficiency

3.2.1 Weight loss measurements

To determine the optimal concentration of corrosion inhibitors based on aqueous suspensions of MgO nanopowders for CS 65 Mn, gravimetric analysis was employed. The study utilized aqueous suspensions of MgO powders at the following mass concentrations: 0.2 wt.%, 0.4 wt.%, 0.6 wt.%, 0.8 wt.%, and 1.0 wt.%. The corrosive medium consisted of a mixture of HNO_3:HCl:H_2O in a 3:2:5 volume ratio. The results are presented in Figure 4.

The gravimetric data illustrate the kinetics of weight loss for 65 Mn CS coupons exposed to the aggressive acidic environment both in the absence and presence of the inhibitor suspensions (Fig. 4a, b). A comparative analysis of the weight loss curves reveals that all tested suspensions significantly reduce the corrosion rate compared to the uninhibited control. However, the efficacy of inhibition varies depending on both the synthesis method of MgO nanopowder and its concentration in the suspension.

The suspension formulated with MgO synthesized via the sol-gel method demonstrated superior protective performance across all concentrations. This is quantitatively supported by the calculated average corrosion rates ($\bar{v}$) and inhibition efficiencies (η), summarized in Table 2. The highest inhibition efficiencies for S-GS-MgO were observed at 0.2 wt.% (η = 48.62%) and 0.4 wt.% (η = 49.15%), indicating a peak performance within this low-concentration range. A further increase in inhibitor loading led to a noticeable decline in efficiency, with values dropping to approximately 22% at 0.6-1.0 wt.%. This suggests a saturation effect or potential agglomeration at higher concentrations, which may compromise the formation of a uniform protective layer.

A similar concentration-dependent trend was observed for the microwave-assisted synthesis suspension, though with overall lower inhibition efficiencies. The maximum efficiency for MAS-MgO was 42.82% at 0.4 wt.%, confirming this concentration as optimal for both types of inhibitors under these experimental conditions. The superior performance of S-GS-MgO is attributed to its higher phase purity, as established by XRD analysis (Fig. 1). The S-GS-MgO sample contained less than 5 wt.% of the $NaNO_3$ impurity phase, compared to approximately 15 wt.% in the MAS-MgO sample. Impurities can act as defects in the protective layer, facilitating localized corrosion and thereby reducing the overall inhibition efficiency.

The residual relative mass of the steel coupons, plotted as a function of inhibitor concentration in Figure 4 c, d, provides a direct visualization of the protective effect. The data unequivocally show that for both inhibitors, the highest residual mass, and thus the greatest protection, is achieved at a concentration of 0.4 wt.%. This concentration is therefore identified as the optimal dosage for maximizing corrosion inhibition efficiency for both MgO nanopowders in the given acidic medium. The subsequent decrease in residual mass at higher concentrations (0.6-1.0 wt.%) further corroborates the conclusion that exceeding the optimal concentration does not enhance protection and may even be detrimental due to changes in the suspension's colloidal stability or adsorption behavior.

The optimal concentration of 0.4 wt.%, identified in the accelerated mixed-acid medium, was subsequently applied for electrochemical characterization in 0.1 M HCl and 0.1 M NaCl. While the absolute inhibition efficiency can be medium-dependent, the consistent observation of a performance maximum at this concentration across both MgO types in the gravimetric test justified its selection as a representative point for comparative mechanistic studies. This approach aligns with standard practice where an optimal concentration identified in an aggressive screening environment is validated in more application-relevant conditions [24, 25]. The subsequent electrochemical data in 0.1 M HCl/NaCl confirmed the significant protective effect of this dosage and allowed for a dissection of the inhibition mechanisms in these specific environments.

3.2.2 Potentiodynamic polarization (PDP) measurements

To quantitatively assess the influence of MgO nanoparticles, synthesized via MAS and S-GS methods, on the corrosion kinetics of CS 65 Mn, potentiodynamic polarization measurements were conducted in two environments: 0.1 M HCl and 0.1 M NaCl. Based on preliminary gravimetric studies, an optimal inhibitor concentration of 0.4 wt.% MgO suspension was selected for detailed electrochemical analysis.

The potentiodynamic polarization curves, presented in Figure 5, demonstrate a significant influence of MgO nanoparticles introduction on the electrochemical behavior of the steel. A pronounced suppression of both anodic and cathodic processes is observed in both corrosive environments. The shift of both branches of the curves towards lower current densities upon the addition of inhibitors indicates a mixed inhibition mechanism. This suggests that MgO nanoparticles adsorb onto the active centers of the steel surface, blocking both anodic and cathodic sites, and form a protective barrier layer [26]. Quantitative parameters extracted from the polarization curves using the Tafel extrapolation method are summarized in Table 3. The key indicator is the corrosion current density (i_{corr}), which is directly proportional to the corrosion rate. In 0.1 M HCl (Table 3), the i_{corr} value for the uninhibited sample was 0.615×10^{-3} mA/cm². The introduction of inhibitors led to its substantial reduction: to 0.385×10^{-3} mA/cm² for MAS-MgO and to 0.227×10^{-3} mA/cm² for S-GS-MgO. Accordingly, the inhibition efficiency (η_{pdp}), calculated using formula (3), reached 59.77% and 63.14% for the MAS and S-GS methods, respectively. The more pronounced protective effect of S-GS-MgO in HCl, despite its larger particle size (~60 nm compared to ~15 nm for MAS-MgO), can be explained by two main factors identified during powder characterization: higher phase purity and, consequently, better adsorption capacity. The presence of a significant amount of $NaNO_3$ impurity (~15 wt.%) in the MAS-MgO sample may negatively affect the stability and homogeneity of the formed protective layer, which is consistent with data from other studies indicating that impurities can act as centers for localized corrosion [23]. Furthermore, in the highly acidic HCl environment, the larger S-GS-MgO particles possibly form a more stable and continuous physical barrier, less susceptible to rapid chemical dissolution.

In 0.1 M NaCl the inhibitory efficiency of MgO nanoparticles was significantly higher. The η_{pdp} values were 73.43% for MAS-MgO and 89.12% for S-GS-MgO. This substantial increase in efficiency compared to HCl is expected and has a clear explanation from the perspectives of thermodynamics and corrosion mechanism. In a neutral environment, magnesium oxide is more stable and less prone to chemical dissolution. This allows it to perform its barrier function longer and more effectively. In the chloride environment, besides the barrier mechanism, an adsorptive neutralizing action may play a dominant role [27]. MgO particles adsorbing on the surface locally increase the pH of the solution's boundary layer through reaction with water. This promotes passivation of the steel surface and hinders the initiation process of pitting corrosion, which is typical for chloride-containing environments.

The shift in corrosion potential (E_{corr}) also provides valuable information. In NaCl, the addition of S-GS-MgO causes a significant anodic shift in E_{corr} of ~174 mV (from -584 mV to -410 mV), which may indicate a predominantly anodic inhibition mechanism in this environment, whereby the inhibitor primarily suppresses the metal dissolution reaction. For MAS-MgO, the shift is also anodic but less pronounced (~97 mV). In HCl, the E_{corr} shifts are less unambiguous: a small anodic shift is observed for S-GS-MgO, while a cathodic shift is noted for MAS-MgO, confirming the mixed type of action. The obtained inhibition efficiency values for MgO (~60-90% in NaCl) are in good agreement with literature data for inorganic nano-inhibitors. For instance, it is reported that ZnO and SiO_2 nanoparticles at similar concentrations demonstrate efficiencies in the range of 70-85% in neutral chloride environments [28, 29]. The advantage of S-GS-MgO demonstrated in this study underscores the critical importance not only of particle size but also of their phase purity and chemical stability for achieving maximum protective effect.

3.3 Corrosion inhibition mechanism study

3.3.1. Electrochemical impedance spectroscopy technique

To gain deeper insight into the interfacial processes and the protective mechanisms afforded by the synthesized MgO nanoparticles, electrochemical impedance spectroscopy was employed. This technique is highly sensitive to changes at the electrode/electrolyte interface, allowing for the characterization of charge transfer resistance, double-layer properties, and the formation of surface films [30]. Results of electrochemical impedance spectroscopy tests on 65 Mn CS before and after the application of corrosion inhibitors in 0.1 M HCl and 0.1 M NaCl solutions are shown in Figure 6. The curves simulated using the ZView software showed good agreement with the experimental data. The electrochemical parameters obtained by fitting the equivalent circuits are statistically presented in Table 4.

The impedance data were analyzed using the equivalent electrical circuit model, shown in Figure 7a. This model is commonly employed to characterize a charge-transfer-controlled corrosion process at a heterogeneous electrode-electrolyte interface [31]. The model consists of the solution resistance (R_s) in series with a parallel combination of the charge transfer resistance (R_{ct}) and a constant phase element (CPE_{dl}). The CPE is used instead of an ideal capacitor to account for the non-ideal capacitive behavior arising from surface roughness, inhomogeneous current distribution, or porosity of the interfacial layer. The physical meaning of the *CPE* parameters (Y_0 and n) is directly linked to the double-layer properties, and the effective capacitance (C_{dl}) was calculated using Brug's formula (Eq. 5) to enable a quantitative discussion of interfacial changes.

The impedance response of the uninhibited steel (blank) in 0.1 M HCl (Fig. 6 a, b) is characterized by a single, depressed capacitive loop, typical of a charge transfer-controlled corrosion process [31]. The relatively low charge transfer resistance (R_{ct} = 37.2 Ohm·cm²) and high double-layer capacitance (C_{dl} =630.5 μF cm⁻²) indicate a highly active surface with facile charge transfer and a thin, non-protective interfacial layer. The introduction of MgO nanopowders significantly alters the impedance response. For both inhibitors, the diameter of the capacitive loop increases substantially, reflecting a higher impedance to the corrosion process. The R_{ct} values rise to 123.3 Ohm·cm² and 146.1 Ohm·cm² for MAS-MgO and S-GS-MgO, respectively. Concurrently, the C_{dl} values decrease markedly to approximately 123-378 μF·cm⁻². This inverse relationship between R_{ct} and C_{dl} is a classic indicator of effective corrosion inhibition [32]. The decrease in C_{dl} can be attributed to either a reduction in the local dielectric constant or an increase in the thickness of the electrical double layer, both resulting from the displacement of water molecules and aggressive ions by adsorbed inhibitor particles forming a protective layer on the metal surface [33]. The constant phase element exponent n remains close to 0.85 for the inhibited samples, suggesting a slightly heterogeneous surface but one that is significantly more capacitive than the blank, consistent with the formation of a protective film.

The superior performance of S-GS-MgO in the acidic medium, as evidenced by its higher R_{ct}, aligns with its higher phase purity identified by XRD. The presence of $NaNO_3$ impurities (~15 wt.%) in MAS-MgO likely introduces defects in the adsorbed layer, compromising its barrier properties and leading to a marginally lower R_{ct} compared to the purer S-GS-MgO. This observation underscores the critical influence of synthetic by-products on the interfacial integrity of nano-inhibitors [34]. In the neutral 0.1 M NaCl environment (Fig. 6 c, d), the impedance behavior reflects a different corrosion scenario, predominantly driven by chloride-induced pitting. The blank sample exhibits a larger R_{ct} (392.1 Ohm·cm²) compared to the acidic medium, which is characteristic of the slower corrosion kinetics in neutral solutions. However, the lower n value (0.64) suggests significant surface inhomogeneity, likely due to the initiation of localized attack [35].

The addition of MgO nanoparticles in NaCl results in a further increase in R_{ct}, reaching 475.2 Ohm·cm² and 486.6 Ohm·cm² for MAS-MgO and S-GS-MgO, respectively. The inhibition efficiencies calculated from EIS data are notably higher than in HCl, corroborating the PDP findings. This enhanced performance in neutral media can be mechanistically explained by a dual action of MgO. Firstly, the nanoparticles act as a physical barrier, blocking active sites on the steel surface. Secondly, and more importantly in a neutral-chloride context, MgO can undergo hydrolysis at the interface, leading to a localized increase in pH in the confined boundary layer. This alkalinization promotes the formation of a more stable passive film (e.g., Fe_2O_3/Fe_3O_4) on the steel surface, thereby increasing its resistance to chloride penetration and pitting initiation [36, 37]. The more pronounced anodic shift in E_{corr} observed in PDP for S-GS-MgO in NaCl supports this mechanism, indicating a stronger influence on the anodic (dissolution) reaction. The C_{dl} values for the inhibited samples in NaCl remain comparable to or slightly lower than that of the blank (Table 4), which is consistent with the formation of a protective surface layer. The n values for inhibited samples remain below 0.75, indicating that the surface, while protected, retains a degree of heterogeneity, possibly due to the particulate nature of the inhibitor layer.

Based on the above experimental results, we draw a schematic diagram of the working principle of the corrosion inhibitors as shown in Figure 7. The impedance behavior of all systems was satisfactorily described by the same equivalent electrical circuit (Fig. 7 a), indicating a unified type of charge transfer-controlled electrochemical process across all scenarios. However, quantitative changes in the circuit parameters reveal key differences in the protective mechanisms. In the absence of an inhibitor, the steel surface undergoes rapid and uniform attack. In 0.1 M HCl (Fig. 7 a), the anodic dissolution of iron and the cathodic hydrogen evolution reaction proceed unimpeded. In 0.1 M NaCl (Fig. 7 d), the primary threat is localized pitting corrosion, where chloride ions adsorb at specific site. The introduction of microwave-synthesized MgO nanoparticles provides a protective effect, albeit compromised. The smaller, defect-rich MAS-MgO particles adsorb onto the steel surface, forming a discontinuous barrier layer. In HCl (Fig. 7 b), this layer partially blocks active sites, retarding both anodic and cathodic reactions. However, the high impurity content ($NaNO_3$) creates defects in the adsorbed layer, allowing localized penetration of H^+ and Cl^- ions. In NaCl (Fig. 7 e), the particles similarly act as a physical barrier. Their smaller size allows for denser packing but offers less effective coverage per particle. A modest interfacial pH increase due to MgO hydrolysis provides some supplementary anodic inhibition. The sol-gel synthesized MgO nanoparticles demonstrate a superior and more robust protective mechanism. Their larger size and higher phase purity enable the formation of a more coherent, stable, and continuous film on the steel surface. In HCl (Fig. 7 c), this film acts as an effective mixed-type inhibitor, providing superior barrier protection by more completely isolating the metal from the aggressive electrolyte. In NaCl (Fig. 7 f), the S-GS-MgO film excels through a dual mechanism: it forms an effective physical barrier against chloride ion ingress, and its stability and basic nature facilitate a more pronounced localized increase in the interfacial pH. This alkalinization promotes the formation and stabilization of a passive oxide layer (e.g., Fe_2O_3/Fe_3O_4) on the steel substrate, significantly enhancing resistance to pitting initiation and propagation, thereby explaining its predominantly anodic inhibition behavior. In summary, the schematic underscores the critical *structure-property-performance* relationship: the synthesis pathway dictates nanoparticle architecture and purity, which in turn govern the dominant inhibition mechanism – from a compromised barrier function in acid for impure MAS-MgO to an effective barrier-plus-passivation mechanism in neutral chloride media for the pure, well-structured S-GS-MgO.

4. Conclusion

This study conclusively establishes that the synthesis pathway is a decisive design parameter for engineering MgO nanoparticle corrosion inhibitors, directly governing their structural characteristics and subsequent protective performance. Sol-gel synthesis yielded larger (~63 nm), more stoichiometric particles with superior phase purity (<5 wt.% impurity), whereas microwave-assisted synthesis produced smaller (~16 nm), defect-rich nanoparticles with significant $NaNO_3$ impurity (~15 wt.%).

These structural differences dictated the dominant inhibition mechanism: the purer S-GS-MgO formed a more effective and stable protective layer, achieving superior inhibition efficiencies of 63.1% in 0.1 M HCl and 89.1% in 0.1 M NaCl, outperforming MAS-MgO (59.8% and 73.4%, respectively). Electrochemical analysis confirmed that S-GS-MgO facilitates a more robust barrier in acidic media and enhances passivation via interfacial pH modification in NaCl environments. The work validates a critical *structure-property-performance* triad, providing a foundational framework for the rational design of nano-inhibitors targeted for specific corrosive threats.

Credit authorship contribution statement

Lingru Zhong: Writing – original draft, Methodology, Writing – review and editing.
Oksana Dubinina: Writing – review and editing, Conceptualization, Supervision, conceptualization, visualization.

Declaration of Competing interest

The authors declare that they have no known competing financial interests or personal relationships that could have appeared to influence the work reported in this paper.

Acknowledgements

«The research was carried out using the equipment of the Center for Sharing Use «Nanomaterials and Nanotechnologies» of Tomsk Polytechnic University supported by the RF Ministry of Education and Science project #075-15-2021-710».

References

[1] Koch, G., Varney, J., Thompson, N., et al. “International measures of prevention, application, and economics of corrosion technologies (IMPACT report)”, NACE International, 2021. http://impact.nace.org/documents/Nace-International-Report.pdf.
[2] Ganjoo, R., Sharma, S., Shabbirbhai, B., et al. “Ionic liquids as green and sustainable corrosion inhibitors II”, in *Eco-Friendly Corrosion Inhibitors*, pp. 391-410, 2022. https://doi.org/10.1016/B978-0-323-91176-4.00008-8.
[3] Dehghani, A., Bahlakeh, G., and Ramezanzadeh, B. “Green eucalyptus leaf extract: a potent source of bio-active corrosion inhibitors for mild steel”, *Bioelectrochemistry*, 130, 107339, 2019. https://doi.org/10.1016/j.bioelechem.2019.107339.
[4] Oreko, B. and Okuma, S. “Recent advances in nanoparticle-based corrosion inhibition of metals: a review”, *NIPES - Journal of Science and Technology Research*, 7(3), pp. 245-265, 2025. https://doi.org/10.37933/nipes/7.3.2025.1449.
[5] Etsuyankpa, B., Hassan, I., Musa, S., et al. “Comprehensive review of recent advances in nanoparticle-based corrosion inhibition approaches”, *Journal of Applied Sciences and Environmental Management*, 28(8), pp. 2269-2286, 2024. https://doi.org/10.4314/jasem.v22i8.1.
[6] Syed Khadar, Y., Surendhiran, S., Gowthambabu, V., et al. “Enhancement of corrosion inhibition of mild steel in acidic media by green-synthesized nano-manganese oxide”, *Materials Today: Proceedings*, 48(4), pp. 889-893, 2021. https://doi.org/10.1016/j.matpr.2021.04.335.
[7] Gapsari, F., Sharma, S., Hadisaputra, S., et al. “Assessing the newly synthesized bio-based amylase-chitosan/cellulose nanocrystals-ZnO composite for enhanced corrosion protection of carbon steel in acidic medium”, *Materials Today Communications*, 44, 112036, 2025. https://doi.org/10.1016/j.mtcomm.2025.112036.
[8] Dubinina, O. and Ilela, A. “The role of steel surface topography in the performance of nanostructured corrosion inhibitors”, *Transactions of the Indian Institute of Metals*, 78, 225, 2025. https://doi.org/10.1007/s12666-025-03746-0.
[9] Bilecka, I. and Niederberger, M. “Microwave chemistry for inorganic nanomaterials synthesis”, *Nanoscale*, 2(8), pp. 1358-1374, 2010. https://doi.org/10.1039/b9nr00377k.
[10] Sim, T., Gençaslan, M., and Merdan, M. “Synthesis of MgO nanoparticles via the sol-gel method for antibacterial applications, investigation of optical properties and comparison with commercial MgO”, *Discover Applied Sciences*, 6, 577, 2024. https://doi.org/10.1007/s42452-024-06299-x.
[11] Thakur, A., Zarrouk, A., Selvaraj, M., et al. “Nanomaterial-based smart coatings for sustainable corrosion protection in harsh marine environments: advances in environmental management and durability”, *Inorganic Chemistry Communications*, 176, 114208, 2025. https://doi.org/10.1016/j.inoche.2025.114280.
[12] Sandhu, G., Nine, M., Purasinhala, K., et al. “Morphology and charge effect of ZnO nanostructures on the performance of anticorrosion coatings”, *Surfaces and Interfaces*, 69, 106750, 2025. https://doi.org/10.1016/j.surfin.2025.106750.
[13] Hemmami, H., Amor, I., Zeghoud, S., et al. “A systematic review of synthesis MgO nanoparticles and their applications”, *Journal of the Turkish Chemical Society*, 11(2), pp. 731-755, 2025. https://doi.org/10.18596/jotcsa.1247385.
[14] Zhao, S., Jing, Y., Liu, T., et al. “Corrosion behavior and mechanism of carbon steel in industrial circulating cooling water system operated by electrochemical descaling technology”, *Journal of Cleaner Production*, 434, 139817, 2024. https://doi.org/10.1016/j.jclepro.2023.139817.
[15] Sanni, O., Fayomi, O., and Popoola, P. “Eco-friendly inhibitors for corrosion protection of stainless steel: an overview”, *Journal of Physics: Conference Series*, 1378(4), 042047, 2019. https://doi.org/10.1088/1742-6596/1378/4/042047.
[16] Brunauer, S., Emmett, P., and Teller, E. “Adsorption of gases in multimolecular layers”, *Journal of the American Chemical Society*, 60(2), pp. 309–319, 1938. https://doi.org/10.1021/ja01269a023.
[17] Xu, R. *Particle characterization: light scattering methods*, Springer Science & Business Media, Dordrecht, 2002. https://doi.org/10.1007/0-306-47124-8.
[18] Suryanarayana, C. and Norton, M. *X-ray diffraction: a practical approach*, Springer, 1998. https://doi.org/10.1007/978-1-4899-0148-4.

[19] ASTM G1-03. “Standard practice for preparing, cleaning, and evaluating corrosion test specimens”, ASTM International, West Conshohocken, PA, 2017. https://doi.org/10.1520/G0001-03R17.

[20] ASTM G59-97. “Standard test method for conducting potentiodynamic polarization resistance measurements”, ASTM International, West Conshohocken, PA, 2020. https://doi.org/10.1520/G0059-97R20.

[21] ASTM G106-89. “Standard practice for verification of algorithm and equipment for electrochemical impedance measurements”, ASTM International, West Conshohocken, PA, 2015. https://doi.org/10.1520/G0106-89R15.

[22] Hirschorn, B., Orazem, M., Tribollet, B., et al. “Determination of effective capacitance and film thickness from constant-phase-element parameters”, *Electrochimica Acta*, 55(21), pp. 6218-6227, 2010. https://doi.org/10.1016/j.electacta.2009.10.065.

[23] Hosseini, M., Ehteshamzadeh, M., and Shahrabi, T. “Protection of mild steel corrosion with Schiff bases in 0.5 M H_2SO_4 solution”, *Electrochimica Acta*, 52(11), pp. 3680-3685, 2007. https://doi.org/10.1016/j.electacta.2006.10.041.

[24] Hao, L., Cai, X., Chen, T., et al. “Corrosion behavior of 650 MPa high strength low alloy steel in industrial polluted environments containing different concentrations of Cl^-”, *International Journal of Minerals, Metallurgy and Materials*, 33(1), pp. 228-241, 2026. https://doi.org/10.1007/s12613-025-3135-5.

[25] Liu, J., Wang, B., Chen, T., et al. “The effect of corrosion inhibitors on the corrosion behavior of ductile cast iron”, *Metals*, 15(1), 70, 2025. https://doi.org/10.3390/met15010070.

[26] Alao, A., Popoola, A., and Sanni, O. “The influence of nanoparticle inhibitors on the corrosion protection of some industrial metals: a review”, *Journal of Bio- and Tribo-Corrosion*, 8, 68, 2022. https://doi.org/10.1007/s40735-022-00665-1.

[27] Li, S., Gao, B., Tu, G., et al. “Effects of magnesium on the microstructure and corrosion resistance of Zn-55Al-1.6Si coating”, *Construction and Building Materials*, 71, pp. 124-131, 2014. https://doi.org/10.1016/j.conbuildmat.2014.08.023.

[28] Yang, G., Zeng, L., Shen, H., et al. “Unveiling the corrosion evolution and pitting mechanism of X70 pipeline steel in typical near-neutral/bentonite soil environment”, Journal of Materials Science & Technology, 243 (4), pp. 149-166. https://doi.org/10.1016/j.jmst.2025.05.010.

[29] Naderi, R. and Attar, M. “The role of zinc aluminum phosphate anticorrosive pigment in the corrosion protection of epoxy coating”, *Corrosion Science*, 52(5), pp. 637-645, 2010. https://doi.org/10.1016/j.corsci.2009.12.019.

[30] Ji, G., Anjum, S., Sundaram, S., et al. “Musa paradisica peel extract as green corrosion inhibitor for mild steel in HCl solution”, *Corrosion Science*, 90, pp. 107-117, 2015. https://doi.org/10.1016/j.corsci.2014.10.002.

[31] Zea, C., Alcántara, J., Barranco-García, R., et al. “Anticorrosive behavior study by localized electrochemical techniques of sol-gel coatings loaded with smart nanocontainers”, *Journal of Coatings Technology and Research*, 14, pp. 841-850, 2017. https://doi.org/10.1007/s11998-017-9936-3.

[32] Orazem, M. and Tribollet, B. *Electrochemical impedance spectroscopy*, John Wiley & Sons, 2017. https://doi.org/10.1002/9781119363682.

[33] Toghan, A., Khairy, M., and Huang, M. “Electrochemical, chemical and theoretical exploration of the corrosion inhibition of carbon steel with new imidazole-carboxamide derivatives in an acidic environment”, *International Journal of Electrochemical Science*, 18(3), 100072, 2023. https://doi.org/10.1016/j.ijoes.2023.100072.

[34] Solomon, M. and Umoren, S. “Enhanced corrosion inhibition effect of polypropylene glycol in the presence of iodide ions at mild steel/saline water interface”, *Journal of Environmental Chemical Engineering*, 5(1), pp. 197-207, 2017. https://doi.org/10.1016/j.jece.2015.05.018.

[35] Liu, C., Bi, Q., Leyland, A., et al. “An electrochemical impedance spectroscopy study of the corrosion behaviour of PVD coated steels in 0.5 N NaCl aqueous solution: part II. EIS interpretation of corrosion behavior”, *Corrosion Science*, 45(6), pp. 1257-1273, 2003. https://doi.org/10.1016/S0010-938X(02)00214-7.

[36] Jing, C., Dong, B., Raza, A., et al. “Corrosion inhibition of layered double hydroxides for metal-based systems”, *Nano Materials Science*, 3(1), pp. 47-67, 2021. https://doi.org/10.1016/j.nanoms.2020.12.001.

[37] Aguilar-Barrientos, J., Pech-Canul, M., and Fernández-Herrera, M. “Corrosion inhibition of carbon steel in neutral chloride solutions using salts of primary bile acids”, *ACS Omega*, 9(39), pp. 40980-40991, 2024. https://doi.org/10.1021/acsomega.4c06362.

Biographies

Zhong Lingru is a materials engineer specializing in nanotechnology applications. She earned her M.Sc. in Materials Science from Tomsk Polytechnic University. Her academic background provides her with a solid foundation in materials science, specific expertise in data analysis and experimental results. Her research focuses on the application of nanomaterials for steel corrosion protection, demonstrating proficiency in data processing, results interpretation, and performance evaluation. She is driven by a desire to intergate nanotechnology with data-driven methods to improve material properties. She is dedicated to creating sustainable and efficient engineering solutions in the fields of materials engineering and corrosion science.

Oksana Dubinina is an associate professor at the School of Engineering, New Manufacturing Technologies, Materials Science Division, Tomsk Polytechnic University. She has a PhD in chemistry. Her primary research focuses on the design and development of novel, environmentally friendly corrosion inhibitors. The work focuses on formulations based on plant-derived nanomaterials and metal and metal oxide nanoparticles. The goal of her research is to create highly efficient, sustainable protective solutions for carbon steel, contributing to the longevity of advanced materials.

Figure captions

Figure 1. XRD patterns of MgO powders obtained by (a) MAS and (b) S-GS.
Figure 2. TEM images and particle size distributions of MgO powders synthesized by MAS (a, b) and S-GS (c, d).

Figure 3. Volumetric particle size distributions from static light scattering for MAS-MgO (a) and S-GS-MgO (b).
Figure 4. Weight loss kinetics (a, b) and residual relative mass (c, d) of CS 65 Mn in acidic mixture with different concentrations of MAS-MgO (a, c) and S-GS-MgO (b, d).
Figure 5. Potentiodynamic polarization curves for CS 65 Mn in 0.1 M HCl (a) and 0.1 M NaCl (b) with and without 0.4 wt.% MgO inhibitors.
Figure 6. Nyquist (a, c) and Bode (b, d) plots for CS 65 Mn in 0.1 M HCl (a, b) and 0.1 M NaCl (c, d) with 0.4 wt.% MgO inhibitors. Solid lines are fits.
Figure 7. Schematic of inhibition mechanisms: (a) equivalent circuit; interfacial scenarios in 0.1 M HCl (a-c) and 0.1 M NaCl (d-f): (a, d) uninhibited, (b, e) with MAS-MgO, (c, f) with S-GS-MgO.

Table captions

Table 1. Mass fraction of the main chemical elements in CS 65 Mn, %.
Table 2. Weight loss results for CS 65 Mn in HNO_3:HCl:H_2O at 25°C.
Table 3. Results of PDP measurements for CS 65 Mn corrosion.
Table 4. Electrochemical impedance spectroscopy parameters for CS 65 Mn corrosion.

Tables

Table 1. Mass fraction of the main chemical elements in CS 65 Mn, %.

C	Mn	Si	P	S	Fe
0.62-0.70	0.9-1.2	0.17-0.37	< 0.035	< 0.035	remaining

Table 2. Weight loss results of CS 65 Mn in HNO_3:HCl:H_2O at 25°C.

inhibitors		$\overline{v}$, mg·s^{-1}·cm^{-2}	η, %
	–	0.493±0.021	–
MAS-MgO	0.2% wt.	0.302±0.012	.
	0.4% wt.	0	4
	0.6% wt.	0	1
	0.8% wt.	0	1
	1% wt.	0.398±0.016	1
S-GS-MgO	0.2% wt.	0.253±0.011	4
	0.4% wt.	0.251±0.012	4
	0.6% wt.	0	2
	0.8% wt.	0	2
	1% wt.	0	2

Table 3. Results of PDP measurements for CS 65 Mn corrosion.

corrosive medium	inhibitors	i_{corr}, mA·cm^{-2}	$-E_{corr}$, mV	$+\beta_a$, mV	$-\beta_c$, mV	v_{corr}, mm/year	η_{pdp}, %
0.1M HCl	–	0.615±0.031	505±5	178.48±8.92	183.93±9.02	7.21±0.36	–
	0.4% wt. MAS MgO	0.385±0.023	544±5	351.28±7.52	528.94±16.45	4.52±0.23	59.77
	0.4% wt. S-GS MgO	0.227±0.011	484±4	210.48±10.02	408.44±20.42	2.66±0.13	63.14
0.1M NaCl	–	0.048±0.002	584±5	552.86±12.31	330.31±16.52	0.56±0.03	–
	0.4% wt. MAS MgO	0.012±0.001	487±3	263.62±13.82	361.33±18.07	0.15±0.007	73.43
	0.4% wt. S-GS MgO	0.005±0.0004	410±5	178.67±8.93	200.12±10.01	0.06±0.003	89.12

Table 4. Electrochemical impedance spectroscopy parameters for CS 65 Mn corrosion.

corrosive medium	inhibitors	R_s, Ohm·cm^2	CPE_{dl}			R_{ct}, Ohm·cm^2
			Y_0, Ω^{-1} s^n cm^{-2} ×10^{-3}	n	C_{dl}, μF·cm^{-2}	
0.1M HCl	–	4.95±0.11	1.33±0.16	0.87±0.02	630.5±21.2	37.2±3.7

	0.4% wt. MAS MgO	39.26±0.19	0.29±0.04	0.84±0.03	123.7±10.3	1
	0.4% wt. S-GS MgO	31.06±0.23	0.34±0.04	0.83±0.02	134.2±4.3	146.1±14.7
0.1M NaCl	–	2	2.13±0.26	0.64±0.02	377.9±18.5	392.1±17.3
	0.4% wt. MAS MgO	19.85±0.43	1.04±0.13	0.72±0.02	229.9±19.2	475.2±20.1
	0.4% wt. S-GS MgO	16.44±0.35	2.72±0.33	0	373.1±20.5	486.6±22.2

Y_0 – *CPE-T, n – CPE-P.*

Figures

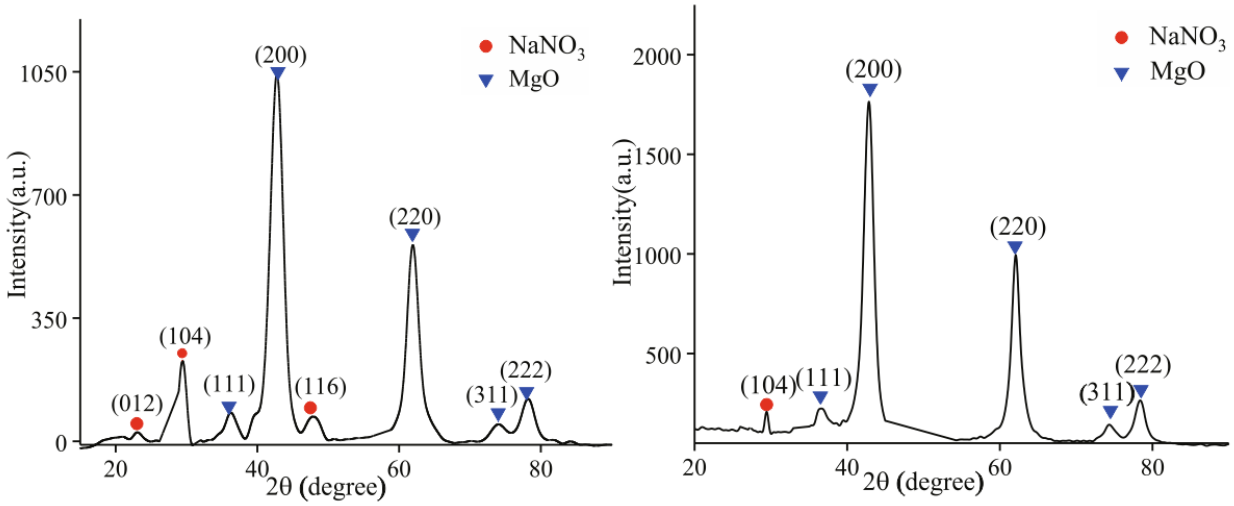

(a) (b)

Figure 1. XRD patterns of MgO powders obtained by (a) MAS and (b) S-GS.

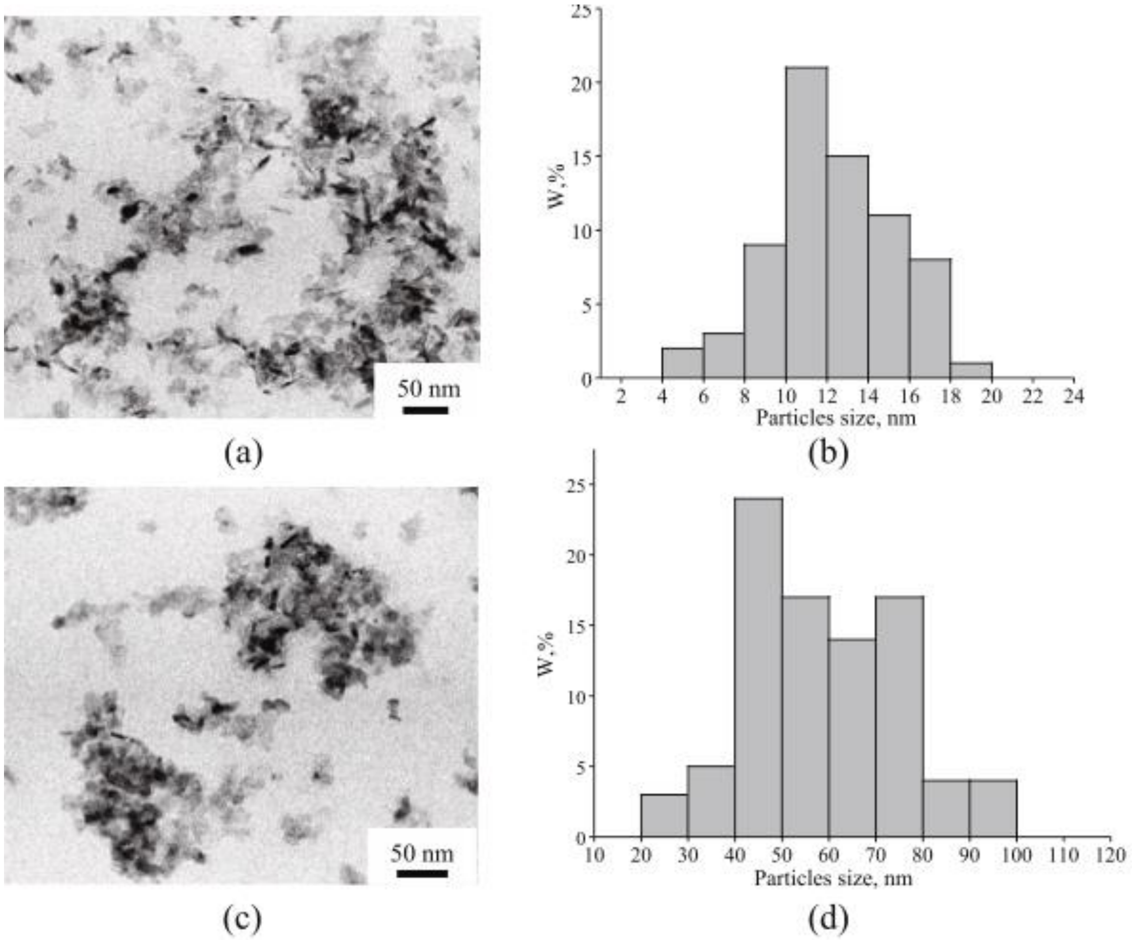

Figure 2. TEM images and particle size distributions of MgO powders synthesized by MAS (a, b) and S-GS (c, d).

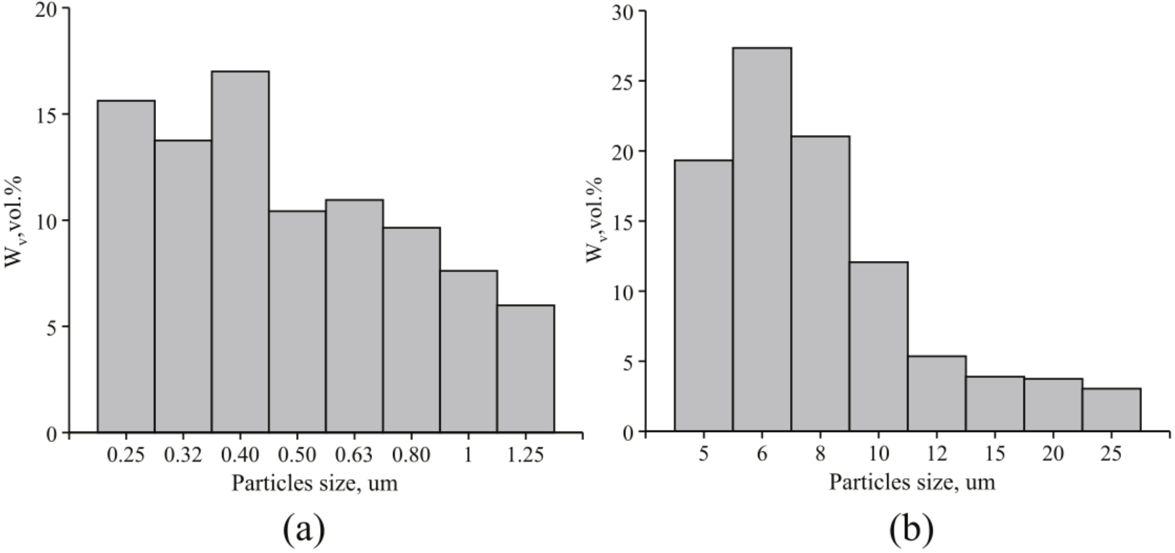

Figure 3. Volumetric particle size distributions from static light scattering for MAS-MgO (a) and S-GS-MgO (b).

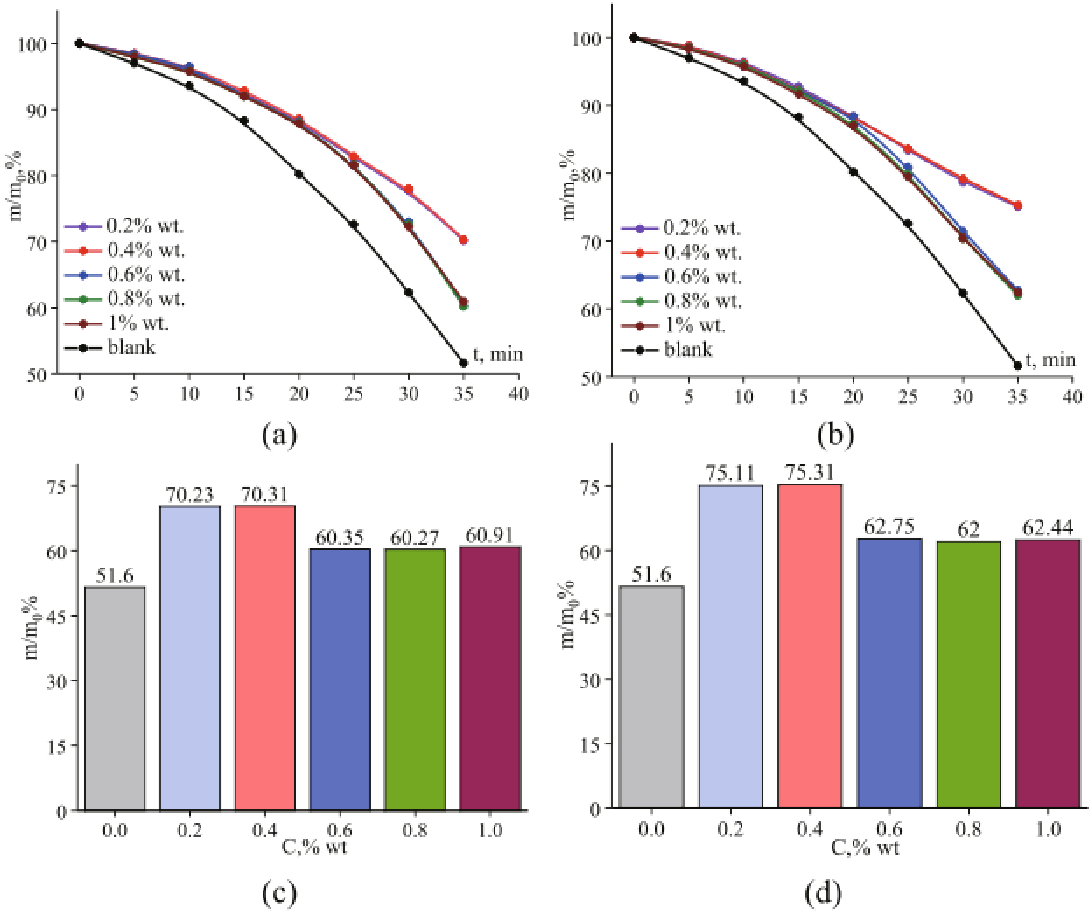

Figure 4. Weight loss kinetics (a, b) and residual relative mass (c, d) of CS 65 Mn in acidic mixture with different concentrations of MAS-MgO (a, c) and S-GS-MgO (b, d).

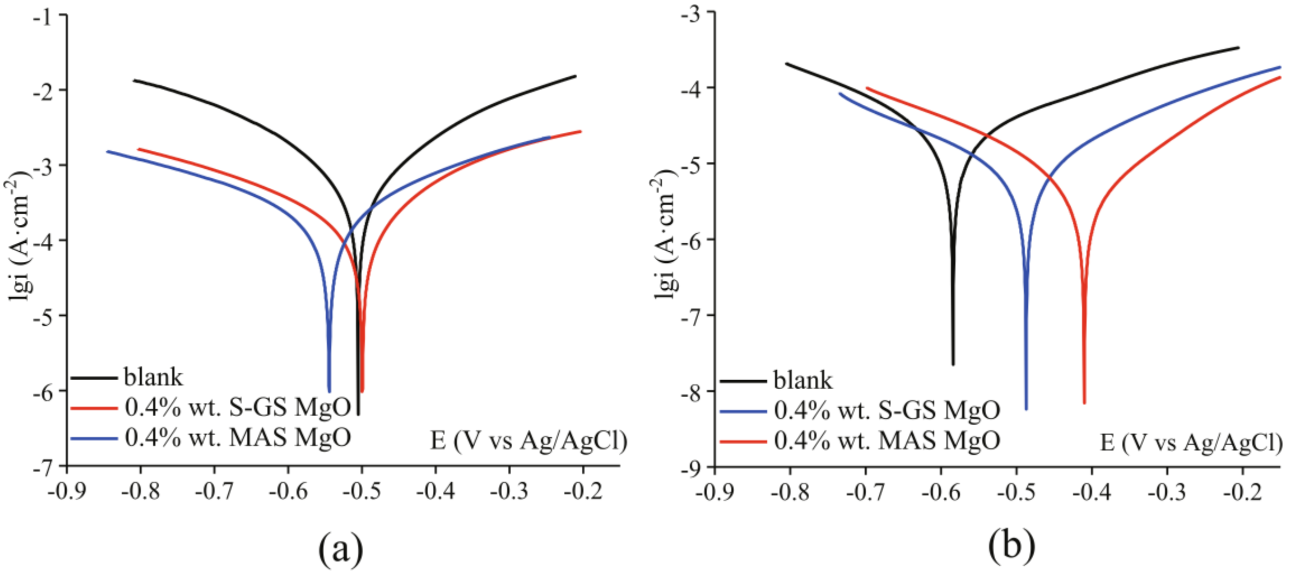

Figure 5. Potentiodynamic polarization curves for CS 65 Mn in 0.1 M HCl (a) and 0.1 M NaCl (b) with and without 0.4 wt.% MgO inhibitors.

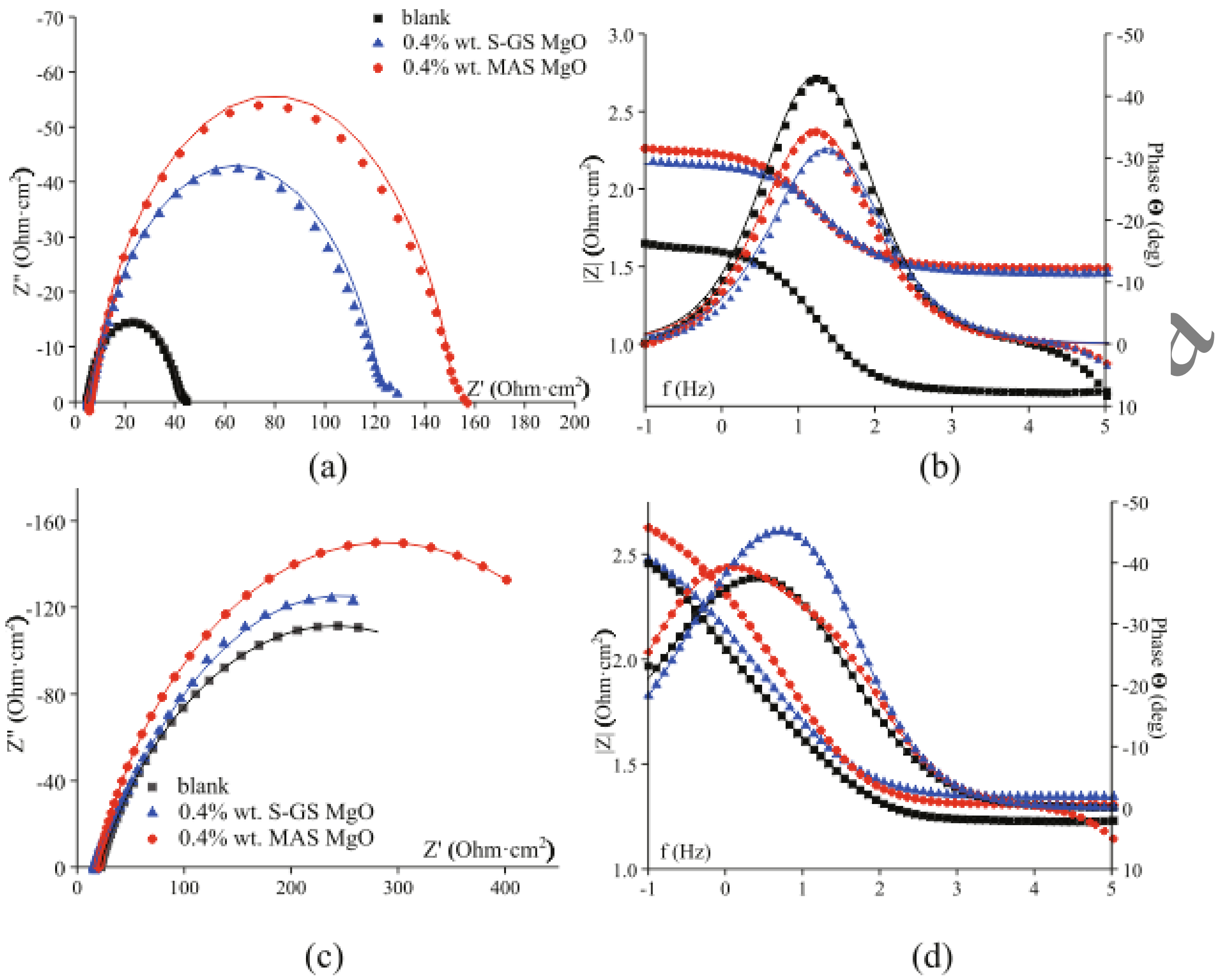

Figure 6. Nyquist (a, c) and Bode (b, d) plots for CS 65 Mn in 0.1 M HCl (a, b) and 0.1 M NaCl (c, d) with 0.4 wt.% MgO inhibitors. Solid lines are fits.

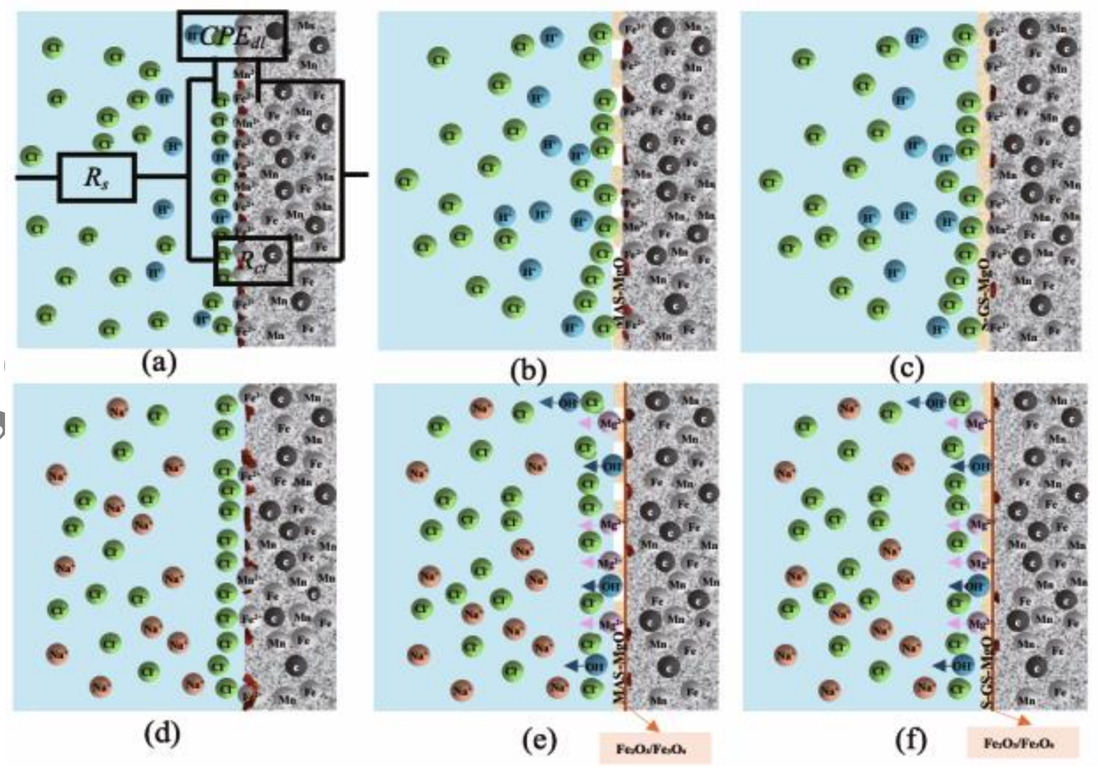

Figure 7. Schematic of inhibition mechanisms: (a) equivalent circuit; interfacial scenarios in 0.1 M HCl (a-c) and 0.1 M NaCl (d-f): (a, d) uninhibited, (b, e) with MAS-MgO, (c, f) with S-GS-MgO.